Monthly Notices of the ROYAL ASTRONOMICAL SOCIETY

MNRAS **507,** 2488–2499 (2021) https://doi.org/10.1093/mnras/stab2341
Advance Access publication 2021 August 13

SDSS-IV MaNGA: Stellar M/L gradients and the M/L-colour relation in galaxies

Junqiang Ge,[1]★ Shude Mao,[2,1] Youjun Lu,[1,3] Michele Cappellari,[4] Richard J. Long[2,5] and Renbin Yan[6]

[1]*National Astronomical Observatories, Chinese Academy of Sciences, 20A Datun Road, Beijing 100101, China*
[2]*Department of Astronomy, Tsinghua University, Beijing 100084, China*
[3]*School of Astronomy and Space Science, University of Chinese Academy of Sciences, Beijing 100049, China*
[4]*Sub-Department of Astrophysics, Department of Physics, University of Oxford, Denys Wilkinson Building, Keble Road, Oxford OX1 3RH, UK*
[5]*Jodrell Bank Centre for Astrophysics, Department of Physics and Astronomy, The University of Manchester, Oxford Road, Manchester M13 9PL, UK*
[6]*Department of Physics and Astronomy, University of Kentucky, 505 Rose Street, Lexington, KY 40506, USA*

Accepted 2021 August 10. Received 2021 August 1; in original form 2021 January 11

ABSTRACT

The stellar mass-to-light ratio gradient in SDSS *r*-band $\nabla(M_*/L_r)$ of a galaxy depends on its mass assembly history, which is imprinted in its morphology and gradients of age, metallicity, and stellar initial mass function (IMF). Taking a MaNGA sample of 2051 galaxies with stellar masses ranging from 10^9 to $10^{12}M_\odot$ released in SDSS DR15, we focus on face-on galaxies, without merger and bar signatures, and investigate the dependence of the 2D $\nabla(M_*/L_r)$ on other galaxy properties, including M_*/L_r-colour relationships by assuming a fixed Salpeter IMF as the mass normalization reference. The median gradient is $\nabla M_*/L_r \sim -0.1$ (i.e. the M_*/L_r is larger at the centre) for massive galaxies, becomes flat around $M_* \sim 10^{10}M_\odot$ and change sign to $\nabla M_*/L_r \sim 0.1$ at the lowest masses. The M_*/L_r inside a half-light radius increases with increasing galaxy stellar mass; in each mass bin, early-type galaxies have the highest value, while pure-disc late-type galaxies have the smallest. Correlation analyses suggest that the mass-weighted stellar age is the dominant parameter influencing the M_*/L_r profile, since a luminosity-weighted age is easily affected by star formation when the specific star formation rate (sSFR) inside the half-light radius is higher than $10^{-3}\,\mathrm{Gyr}^{-1}$. With increased sSFR gradient, one can obtain a steeper negative $\nabla(M_*/L_r)$. The scatter in the slopes of M_*/L-colour relations increases with increasing sSFR, for example, the slope for post-starburst galaxies can be flattened to 0.45 from the global value 0.87 in the M_*/L versus $g-r$ diagram. Hence converting galaxy colours to M_*/L should be done carefully, especially for those galaxies with young luminosity-weighted stellar ages, which can have quite different star formation histories.

Key words: galaxies: elliptical and lenticular, cD – galaxies: evolution – galaxies: formation – galaxies: fundamental parameters – galaxies: spiral – galaxies: star formation.

1 INTRODUCTION

The stellar mass assembly history of a galaxy is one of the key parameters for understanding its formation and evolution processes. An important first step is to understand what the stellar mass of a galaxy is from the observations we take. At optical wavelengths, we define a simple multiplicative relationship between the light received from a galaxy and its mass, the stellar mass-to-light ratio M_*/L. Currently, we have three different ways of estimating the mass-to-light ratios and thus galaxy stellar masses.

The first method involves performing a stellar population analysis on the observed galaxy spectra or broad-band spectral energy distributions (SEDs), and calculating the stellar mass based on fitted weights to a series of stellar population templates with different stellar mass-to-light ratios (M_*/L) (see the review by Conroy 2013).

The second converts the galaxy luminosity (L) at a specific wavelength band to stellar mass by employing an empirical stellar mass-to-light ratio to colour relationship (e.g. Bell et al. 2003; Gallazzi & Bell 2009; Du, Li & Li 2019).

The third method uses dynamical modelling of a galaxy to obtain M_*/L. For simplicity, the ratio is often assumed to be constant over the whole galaxy, and is taken as a free parameter when seeking to reproduce a galaxy's 2D stellar kinematic maps (e.g. Cappellari et al. 2006, 2013; Thomas et al. 2011; Cappellari 2016; Li et al. 2017; Lu et al. 2020).

When applying stellar population analysis to obtain a M_*/L, the accuracy depends on both the fitting algorithm and stellar population models. The empirical M_*/L-colour relation also depends on how well M_*/L can be fitted. In the galaxy dynamical modelling, the stellar masses are not affected by any uncertainties in stellar population analysis, but methods are affected by a stellar and dark matter mass degeneracy and the assumption of a constant M_*/L may not be robust.

In the literature, radial M_*/L gradients of galaxies are mainly obtained from stellar population analyses of spatially resolved spectra or broad-band SEDs by assuming a constant initial mass function (IMF). For example, Tortora et al. (2011) performed SED fitting to SDSS *ugriz* bands and found that the M_*/L gradients vary

★ E-mail: jqge@nao.cas.cn

with galaxy stellar mass. Assuming a fixed IMF, the MaNGA work by Li et al. (2018) (see their fig. 6) found that the M_*/L gradients tend to follow the age gradients: the M_*/L gradient is nearly flat or implies a larger M_*/L in the centre for older galaxies and a larger M/L in the outer parts for younger ones. Massive elliptical galaxies can also have negative M_*/L gradients, e.g. Szomoru et al. (2013), Newman, Ellis & Treu (2015). Sonnenfeld et al. (2018) obtained gradients by using three different methods: $u-g$ colour versus M_*/L relation, $U-B-V$ colours versus M_*/L relation, weak and strong lensing modelling resulting in three different negative values of -0.13, -0.15, and -0.24, respectively. CALIFA (Sanchez et al. 2012) galaxies with morphologies ranging from E0 to Sd types have their M_*/L gradients steeper than -0.2 in the inner regions and nearly flat in the outer regions (García-Benito et al. 2019).

Galaxy M_*/L gradients cannot only be estimated by spatially resolved photometric or spectroscopic data, but also predicted using galaxy formation and evolution models. From theoretical (e.g. White & Rees 1978; Hopkins et al. 2009, 2010; Oser et al. 2010, 2012) and observational (e.g. Bezanson et al. 2009; Naab 2013; Martin-Navarro et al. 2018) studies, the formation and evolution of elliptical and bulge-dominated spiral galaxies usually occur through two distinct phases, i.e. first a 'monolithic' collapse phase to form the '*in situ*' stars (e.g. Eggen, Lynden-Bell & Sandage 1962; Larson 1974), and a second merger-driven growth phase to accrete 'ex situ' stars (e.g. Ciotti, Lanzoni & Volonteri 2007; Oser et al. 2012; Rodriguez-Gomez et al. 2016). This two-phase scenario suggests that these galaxies possibly have varying radial gradients of stellar population parameters, including stellar age, metallicity, and IMF, which are exactly the three parameters that determine a M_*/L from a spectrum.

For early type galaxies (ETGs), including both ellipticals (E) and lenticulars (S0), Kuntschner et al. (2010) and Li et al. (2018) consistently show that the age gradients are nearly flat for older ETGs (see also Zheng et al. 2017; Martin-Navarro et al. 2018), while younger ETGs tend to have younger cores, likely associated to residual star formation in the centres. Gonzalez Delgado et al. (2015) found negative age gradients inside a half-light radius (HLR), but nearly flat ones beyond 2 HLR. Positive age gradients can be obtained by changing the sample and data analysis methods (e.g. Koleva et al. 2011; Tortora et al. 2011; Goddard et al. 2017). For late-type galaxies (LTGs), galaxies with higher stellar masses tend to have steeper negative age gradients, and those with lower masses have their gradients varying from negative, nearly flat, to positive gradients (e.g. Tortora et al. 2011; Pérez et al. 2013; Gonzalez Delgado et al. 2015; Zheng et al. 2017).

Statistically, ETGs and LTGs have negative metallicity gradients in logarithmic radius, with the values ranging from -0.5 to 0 (e.g. Mehlert et al. 2003; Spolaor et al. 2009; Kuntschner et al. 2010; Gonzalez Delgado et al. 2015; Goddard et al. 2017; Zheng et al. 2017; Li et al. 2018; Martin-Navarro et al. 2018; Zibetti et al. 2020).

Evidence of IMF variation has been presented by different authors. Initial convincing evidence for an IMF heavier than the Milky Way's in massive ETGs was inferred by modelling stellar absorption lines by van Dokkum & Conroy (2010). This result appeared consistent with similar evidence from mass determinations using strong lensing (Auger et al. 2010). Dynamical modelling of the Atlas3D sample by Cappellari et al. (2012) indicated a systematic trend in the IMF, going from Milky-Way like in the low velocity dispersion and younger ETGs to Salpeter-like or heavier for the high dispersion and older ETGs. A systematic trend was subsequently also inferred from stellar population analyses by Ferreras et al. (2013), Spiniello et al. (2014), Conroy, van Dokkum & Villaume (2017), Li et al. (2017), Parikh et al. (2018), Vaughan et al. (2018), and Zhou et al. (2019), although some studies found no clear evidence (e.g. Zieleniewski 2017; Alton, Smith & Lucey 2018; Vaughan et al. 2018a). A recent review of the consistency and tension in IMF determination studies is given by Smith (2020).

In this paper, we will use SDSS-IV/MaNGA (Bundy et al. 2015) IFS data to study M_*/L gradients driven by age and metallicity gradients under a fixed Salpeter IMF assumption, and investigate how they affect stellar mass estimations and M_*/L-colour relations. Our spectral fitting code and libraries, and data analysis processes are described in Section 2. We analyse M_*/L gradients and M_*/L-colour relations for MaNGA galaxies based on fixed IMF assumption in Section 3. We compare our results with previous works and discuss the effect of radially varying IMFs to M_*/L measurements and M_*/L-colour relations in Section 4. Our conclusions are summarized in Section 5.

2 GALAXY SAMPLE AND DATA ANALYSIS

2.1 The galaxy sample selection

The SDSS 15th data release (DR15; Aguado et al. 2019) includes 4672 galaxies with MaNGA IFS observations, and also morphological classifications (Domínguez Sánchez et al. 2018) and photometric decompositions (Fischer, Domínguez Sánchez & Bernardi 2019) as well. These value added catalogues (VACs) allow us to understand how galaxies with different morphologies have evolved. We select 2051 face-on viewed (inclination angle $i < 45°$) MaNGA galaxies in total by excluding merging and barred galaxies, and those with minor and major axes ratio $b/a < 0.5$, with the ratios being taken from Fischer et al. (2019).

Using galaxy morphologies classified based on deep learning (Domínguez Sánchez et al. 2018) and the photometric decompositions (Fischer et al. 2019), we divide the galaxies we have selected into three subsamples to aid our analyses: (1) 873 ETGs with Sersic index $n > 2.5$; (2) 668 LTGs with both bulge and disc components (bulge+disc LTGs); and (3) 510 pure disc LTGs without a bulge component and with $n < 2.5$ (pure-disc LTGs).

2.2 PPXF full-spectrum fitting and the SSP library

For our selected MaNGA galaxies, we apply the full-spectrum fitting code PPXF (Cappellari & Emsellem 2004; Cappellari 2017) to the galaxies' IFS data. Using this software, when the spectral signal-to-noise ratio (S/N) is larger than 30, we can obtain stellar population parameters with biases and scatters less than 0.05 dex (Ge et al. 2018). We use the version 6.7.6 of the Python code[1] as taken in our previous works (Ge et al. 2018, 2019) for spectral analyses.

With PPXF selected, an SSP library that can model the evolution of MaNGA galaxies is required. Ge et al. (2019) evaluated the three ingredients used for generating an SSP library: the IMF, stellar evolution isochrones, and the empirical stellar library. It was found that local galaxy evolution was best described by the Vazdekis/MILES model (Vazdekis et al. 2010) with BaSTI isochrones (Pietrinferni et al. 2004; Cordier et al. 2007). For the IMF, it is not possible currently to confirm just how the IMF varies with different galaxies. As reviewed in Section 4.2 of Cappellari (2016), the stellar IMF can vary from a Salpeter IMF (Salpeter 1955) in high mass elliptical galaxies (e.g. Cappellari et al. 2012) to a Chabrier IMF (Chabrier 2003) in low mass spiral galaxies (e.g. Li et al. 2017), with the IMF

[1] Available from https://pypi.org/project/ppxf/

tending to be Kroupa-like (Kroupa 2001) in the outskirts of elliptical galaxies (e.g. Domínguez Sánchez et al. 2019). Given that derived stellar population parameters like age, metallicity, and SFR are only weakly sensitive to a change in the IMF between Chabrier/Kroupa and Salpeter, we adopt the latter as our reference. Any possible radial IMF variation, or IMF variation among galaxies, will produce an offset which should be added to the M_*/L values we derive, but is essentially independent of the gradient measurement. For galaxies with star-forming regions, to cover recent star formation, our youngest age in the SSP is dictated by the limit of the library. Therefore, in this work, we select a subset of 25 logarithmically spaced with ∼0.11 dex sampled ages between 0.06 and 14 Gyr, and 12 metallicities ([M/H] = −2.27, −1.79, −1.49, −1.26, −0.96, −0.66, −0.35, −0.25, 0.06, 0.15, 0.26, 0.4). Following the data analysis process in the next section, the fraction of spectral fittings with the luminosity-weighted age (t_L) younger than 100 Myr is less than 0.04 per cent, for which the spectral fitting might be affected due to the existence of stars with ages younger than 60 Myr. This small fraction will not affect our statistical analyses on M_*/L gradients and M_*/L-colour relations.

With the PPXF code and SSP library, we derive the stellar population parameters and gas related parameters separately. For stellar population parameters, as done in Ge et al. (2019), we perform the PPXF fitting by assuming a uniform dust reddening curve given by Calzetti et al. (2000) to correct the intrinsic dust extinction, with all emission lines masked. For emission line fitting, we re-fit the MaNGA spectra by following the emission line fitting example given in the PPXF package: correct the dust extinction of gaseous emissions with Calzetti's dust extinction curve, but correct the extinction of stellar continuum by adopting a 10-th degree of multi-polynomials (MDEGREE=10), by setting the flux ratio of [O I], [O III], and [N II] doublets fixed at theoretical flux ratio of ∼3, [O II] and [S II] doublets restricted to ratios in the physical range. Considering that not all Balmer lines are detectable especially for ETGs, we allow free flux fitting of Balmer emission lines, but fix their line widths to be the same.

2.3 IFS data analysis

Since the surface brightness of a galaxy decreases with increasing radius, current MaNGA IFS observations can only provide an SDSS r-band, S/N ∼ 1 per spectral pixel at the edge of their field of view (FoV). To improve the robustness of our stellar population analysis results, we first select those spaxels with S/N>2 and spatially rebin them to S/N ∼ 20 using the Voronoi 2d binning method[2] described in Cappellari & Copin (2003). There are 690 944 Voronoi bins in total obtained from the 2051 galaxies, with a median of 245 bins for each galaxy, and a median redshift of $z \sim 0.04$, which corresponds to 0.796 kpc arcsec^{-1}. For the total 690 944 spectra, ∼74 per cent of them have single pixels with S/N > 20, and only ∼3 per cent of them are rebinned from larger than 20 spaxels, which means the diameters of these bins are comparable to or larger than the spatial resolution of MaNGA observations (FWHM = 2.5 arcsec; Bundy et al. 2015). When applying the Voronoi 2D binning method to improve the S/N of spaxels with S/N < 20, the basic assumption for those rebinned spaxels is that they have the same physical properties, since most of them (∼97 per cent) have the size smaller than the spatial resolution of MaNGA observation. For each Voronoi bin, we take the mean spectrum of all the stacked spaxels as the stacked spectrum, with the physical parameters of each spaxel in a spatial bin equal to each other.

After applying the PPXF code with our SSP libraries to these spatially rebinned spectra, by adopting 10th order multiplicative polynomials, we correct for inaccuracies in the spectral calibration and make the resulting data insensitive to reddening by dust (Cappellari 2017). We then determine the stellar kinematic 2D distributions, which are used subsequently to correct galaxy rotation during the radial spectral stacking process.

To study galaxy's M_*/L gradient, we take the M_*/L in the SDSS r-band for analysis, with the definition the same as in equation (2) of Ge et al. (2018)

$$M_*/L_r = \frac{\Sigma f_{M,i}}{\Sigma f_{M,i}/(M_*/L_r)_i}, \quad (1)$$

where M_* of the i-th SSP template includes the mass in living stars and stellar remnants, but excludes the gas lost during stellar evolution. $(M_*/L_r)_i$ corresponds to the r-band M_*/L of the i-th template, and $f_{M,i}$ is the fitted mass fraction. The IFS spaxels of a galaxy are divided into different radial bins based on its ellipticity (or the b/a axial ratio), position angle, and the brightest central spaxel in the SDSS r -band. Considering that the maximum MaNGA FoV of ∼30 arcsec can cover the central $1.5R_e$ for 60 per cent of galaxies and $2.5R_e$ for 30 per cent of galaxies (Yan et al. 2016), we use the Python package MGEFIT[3] by Cappellari (2002) to model a galaxy's surface brightness within its MaNGA FoV (≤30 arcsec). The MGE fitted b/a axial ratio and position angle (rather than values for the whole galaxy) are used to construct radial bins for further spectral stacking or parameter estimations.

With interacting and barred galaxies excluded from our sample, the central brightest spaxel of each galaxy matches the luminosity-weighted galaxy centre well, and is therefore defined as the centre for bin construction. These bins are radial annuli formed by dividing the galaxy's major axis into 1 arcsec intervals. Since the pixel size of MaNGA data is 0.5 × 0.5 arcsec, each radial bin includes two spaxels in the major axis and at least one spaxel (for $b/a = 0.5$) along the minor axis. For each galaxy, there are at most 15 concentric annuli for studying radial gradients in M_*/L_r and the other stellar population parameters. Taking into account the typical seeing of FWHM ∼1.5 arcsec for the MaNGA survey (Bundy et al. 2015), we only use those radial annuli whose radii measured along the major axis are larger than 1.5 arcsec, and the number of annuli with observed spectra is at least 3 for gradient calculations. Considering that the MaNGA survey is designed for mapping nearby galaxies primarily to $1.5R_e$ (Yan et al. 2016), we set the cutoff of maximum radii to $1.5R_e$ for gradient fitting of each galaxy. The minimum radii of the elliptical bins are set to $0.1R_e$ or 1.5 arcsec for galaxies with low spatial resolution, by taking into account the typical seeing (1.5 arcsec) of MaNGA observations.

There are two ways of estimating parameters using the radial annuli: either use the median parameter values from individual spectra, or stack the spectra and then calculate the parameter values. For a particular elliptical bin, we can average each parameter based on all the spaxels included in the radial bin. For the second method, we also obtain the mean spectrum of all spaxels in this bin. Therefore, all quantities derived from the two methods can be comparable to each other. We explain and evaluate both methods, and compare the results obtained. In the first method, after the 2D Voronoi binning, we can perform PPXF fitting on the spectrum associated with each Voronoi bin, and calculate the stellar population parameter values,

[2]Available from https://pypi.org/project/vorbin/

[3]Available from https://pypi.org/project/mgefit/

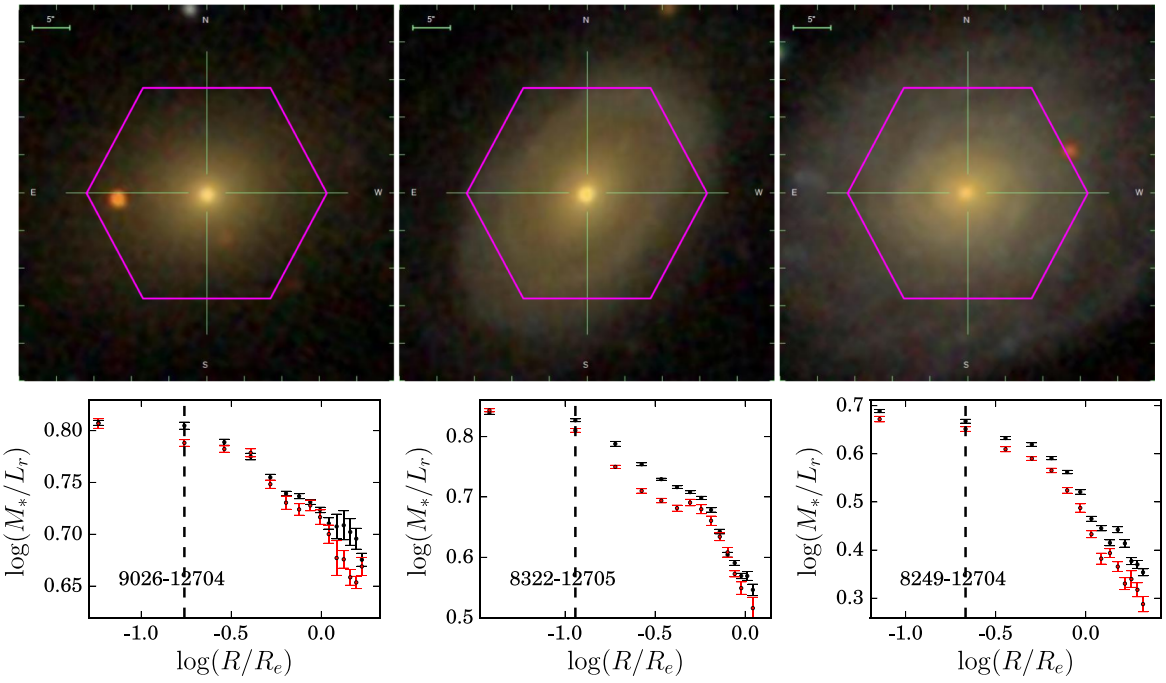

Figure 1. Fitting examples of an ETG (left-hand column), a bulge+disc LTG (middle column), and a pure-disc LTG (right-hand column). The top row shows the SDSS *gri*-bands stacked image for each galaxy with the MaNGA FoV overplotted as a pink hexagon. The bottom three panels show the corresponding radial M_*/L_r variations of each galaxy, in which the black points with error bars are $(M_*/L_r)_{\rm 2Dbin}$ with the values calculated from 2D maps, while those in red represent $(M_*/L_r)_{\rm Rstack}$ with the values obtained from radially stacked spectra. In each bottom panel, the vertical dashed line shows the position of 1.5 arcsec, which is the typical seeing of MaNGA observations.

which can then be binned into the radial annuli. The radial distribution of each parameter (e.g. $(M_*/L_r)_{\rm 2Dbin}$) can be obtained by calculating the median values in each annulus, with the scatter of each parameter being estimated as the root mean square value. In the second method, using the 2D velocity maps determined earlier (with rebinned spectral S/N $\sim$ 20), we bring all the spectra in each radial annulus to the same velocity, i.e. $V_* = 0$ km s^{-1}, and then stack them together. From these stacked spectra in each radial annulus, we can obtain (using PPXF again) the corresponding stellar population parameter values (e.g. $(M_*/L_r)_{\rm Rstack}$).

Fig. 1 shows three examples using both methods: an ETG, a bulge+disc LTG, and a pure-disc LTG. The bottom three panels show radial variations of $(M_*/L_r)_{\rm 2Dbin}$ (black colour) and $(M_*/L_r)_{\rm Rstack}$ (red colour), with the corresponding errors estimated in two different ways. The error bar of $(M_*/L_r)_{\rm 2Dbin}$ is calculated based on all the spaxels in each annulus by assuming each spaxel has the same M_*/L_r uncertainty. For $(M_*/L_r)_{\rm Rstack}$, we obtain its uncertainty from its Monte Carlo based estimation by assuming the flux error of stacked spectra obeys the standard normal distribution. For other surveys with higher spatial resolution, e.g. VLT/MUSE (Bacon et al. 2014), one can obtain more radial bins than the MaNGA case, which means more detailed substructures and possibly larger fluctuation appearing in the radial curve compared to MaNGA observations. As to the gradient fitting, the radial elliptical bins taken in our analysis are 2.5 to 7.5 times larger than the spatial resolution (FWHM) for the MaNGA primary galaxy sample (table 3 of Bundy et al. 2015), which can already support a robust gradient measurement.

As shown in Fig. 1, $(M_*/L_r)_{\rm Rstack} < (M_*/L_r)_{\rm 2Dbin}$ happens at different radii for different types of galaxies. ETGs have increasing differences with larger radii; bulge+disc LTGs have large differences for $\log(R/R_e) \sim [-1.0, -0.2]$ and no significant difference at other radii; and pure-disc LTGs show a systematic decrease in $(M_*/L_r)_{\rm Rstack}$ at all radii.

To have a thorough understanding on the difference between measured $(M_*/L_r)_{\rm Rstack}$ and $(M_*/L_r)_{\rm 2Dbin}$, we compare them directly in the left-hand panel of Fig. 2. By applying the Python code LTS_LINEFIT in version 5.0.18[4] (Cappellari et al. 2013) for correlation analysis, the fitted slope of the correlation for the $\log(M_*/L_r)_{\rm 2Dbin}$ versus $\log(M_*/L_r)_{\rm Rstack}$ plot is 0.919 ± 0.004, which is flatter than the dashed diagonal equality line. At the high M_*/L_r end, the values derived from the two methods are the same to each other, which indicates that for those old spectra without strong SFR, both the two methods can converge to the same results. With decreasing M_*/L_r, the bias of the M_*/L_r measurements increase.

Bias in the two M_*/L_r measurements also introduces a systematic bias to the slopes of radial M_*/L_r gradients for galaxies in our sample as shown in the right-hand panel of Fig. 2. We find that $\nabla(M_*/L_r)_{\rm 2Dbin} = 0.84 \times \nabla(M_*/L_r)_{\rm Rstack} - 0.05$, which is also derived using the Python code LTS_LINEFIT. The fitted slope that is flatter than the diagonal equality line should be mainly caused by the spatially inhomogeneous surface densities of star formation rate (SFR) inside a galaxy. For spaxels in a radial annulus, if their SFRs have large variation, then those spaxels with higher SFRs can contribute a larger luminosity fraction than those with lower SFRs due to the larger luminosity fraction of young and high-mass stars. This makes the spectral fitting to the stacked spectrum biased to smaller M_*/L since young stellar populations with higher luminosity can obscure signals from older ones, hence the derived $(M_*/L_r)_{\rm Rstack}$ is smaller than the corresponding $(M_*/L_r)_{\rm 2Dbin}$. To avoid the possible uncertainties

[4]Available from https://pypi.org/project/ltsfit/

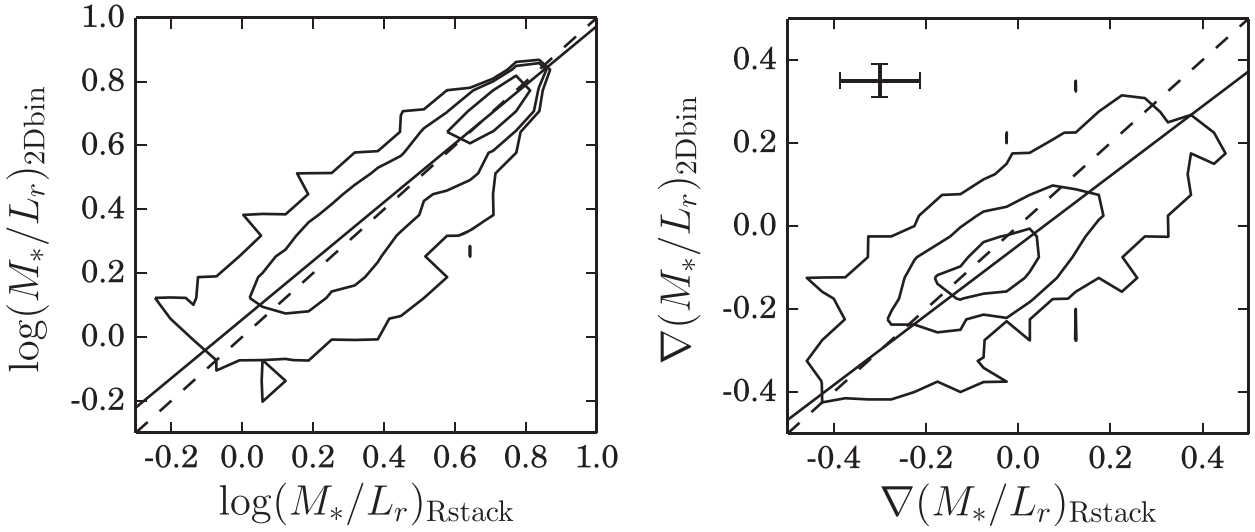

Figure 2. Comparison between two representations of M_*/L_r and their radial gradients, with black contours showing the density distributions of Voronoi rebinned spectra in the left-hand panel and galaxies in the right-hand panel, respectively. Left-hand panel: Corresponding to Fig. 1, $\log(M_*/L_r)_{\rm 2Dbin}$ are systematically higher than $\log(M_*/L_r)_{\rm Rstack}$ at the low M_*/L_r end, with the linear fitting result $\log(M_*/L_r)_{\rm 2Dbin} = 0.919 \times \log(M_*/L_r)_{\rm Rstack} - 0.055$ as shown by the black solid line. Here we use the Python code LTS_LINEFIT (Cappellari et al. 2013) for correlation analysis, the typical errors of $\log(M_*/L_r)_{\rm 2Dbin}$ and $\log(M_*/L_r)_{\rm Rstack}$ are roughly ∼0.01. This correlation has Spearman correlation coefficient $r_s = 0.91$ and Pearson correlation coefficient $r_p = 0.9$. The linear slope 0.919 ± 0.004 with a scatter of 0.061 ± 0.001 is flatter than the dashed diagonal equality line. Right-hand panel: The M_*/L_r difference between the two methods causes a systematic bias to the measured M_*/L_r gradients, with the linear fitting result $\nabla(M_*/L_r)_{\rm 2Dbin} = 0.840 \times \nabla(M_*/L_r)_{\rm Rstack} - 0.047$ shown by the black solid line. The typical errors of $\nabla(M_*/L_r)_{\rm Rstack}$ and $\nabla(M_*/L_r)_{\rm 2Dbin}$ are displayed in the top-left of the right-hand panel. This correlation has Spearman correlation coefficient $r_s = 0.7$ and Pearson correlation coefficient $r_p = 0.73$. The linear slope 0.840 ± 0.013 with a scatter of 0.072 ± 0.004 is flatter than the dashed diagonal equality line.

caused by SFR variation, in this work, we take $(M_*/L_r)_{\rm 2Dbin}$ instead of $(M_*/L_r)_{\rm Rstack}$ for gradient and M_*/L-colour relation analyses.

The gradients are measured by performing a fit of the linear relation

$$\log(M_*/L_r) = a + b \times \log(R/R_e) \tag{2}$$

within the radial range $0.1R_e$ (or 1.5 arcsec for low spatially resolved galaxies) and $1.5R_e$. We define the gradient as the slope of the linear fit $\nabla(M_*/L_r) \equiv b$, and perform the fit using Numpy's (Harris et al. 2020) POLYFIT. The formal errors are calculated from the returned covariance matrix. The gradients of other parameters including luminosity-weighted age $\log(t_L/{\rm yr})$, mass-weighted age $\log(t_M/{\rm yr})$, luminosity-weighted metallicity $[{\rm M/H}]_L$, mass-weighted metallicity $[{\rm M/H}]_M$, dust extinction E(B-V), and the star formation rate (SFR) and specific SFR in logarithms, i.e. log (SFR) and log (sSFR), are defined similarly. The errors in these gradients are estimated using the Python NUMPY (Oliphant 2007) POLYFIT routine.

For each spatially rebinned spaxel, its SFR and sSFR are converted from the PPXF fitted Hα luminosity using the empirical law given by Kennicutt (1998) under the Salpeter IMF assumption,

$${\rm SFR}(M_\odot {\rm yr}^{-1}) = 7.9 \times 10^{-42} L({\rm H}\alpha)\ ({\rm ergs\ s}^{-1}), \tag{3}$$

and the sSFR is defined as

$${\rm sSFR}\ ({\rm Gyr}^{-1}) = {\rm SFR}/M_* \times 10^9. \tag{4}$$

Given that the stellar age, metallicity, SFR, and sSFR of spaxels in ETGs and LTGs can actually cover several order of magnitudes, gradients are calculated logarithmically.

3 RESULTS

We first study the properties of M_*/L_r gradients using a radially fixed Salpeter IMF assumption for galaxies with different morphologies. The results could help understand the evolution of different galaxy types and their resulting gradient distributions. We then introduce radially varying IMFs and consider their impact on the gradients and the relations between M_*/L_r and galaxy colours.

3.1 M_*/L_r gradients for galaxies with different morphologies and the fixed Salpeter IMF assumption

The top panel of Fig. 3 shows the M_*/L_r gradients as a function of stellar mass for three kinds of galaxies: ETGs (red points), bulge+disc LTGs (green points), and pure-disc LTGs (blue points). Here the galaxy stellar mass is estimated by

$$M_*^{\rm tot} = (M_*/L_r)_e \times L_r^{\rm tot}, \tag{5}$$

where $(M_*/L_r)_e$ is the projected stellar mass-to-light ratio inside the half-light radius R_e under the assumption of a constant Salpeter IMF, which is calculated based on the 2D M_*/L_r maps and the corresponding r-band luminosity

$$(M_*/L_r)_e = \frac{\sum_{j=1}^{N} L_{r,j}(M_*/L_r)_j}{\sum_{j=1}^{N} L_{r,j}}, \tag{6}$$

where N is the total number of spaxels inside R_e, and $L_{r,j}$ and $(M_*/L_r)_j$ are the r-band luminosity and M_*/L_r of the jth spaxel, respectively.

This estimate assumes that the $(M_*/L_r)_e$ is representative of the one over the full galaxy, and a better estimate could be obtained if we could directly measure the M_*/L over the full galaxy. However, the MaNGA survey is limited to $1.5R_e$ for most galaxies (Bundy

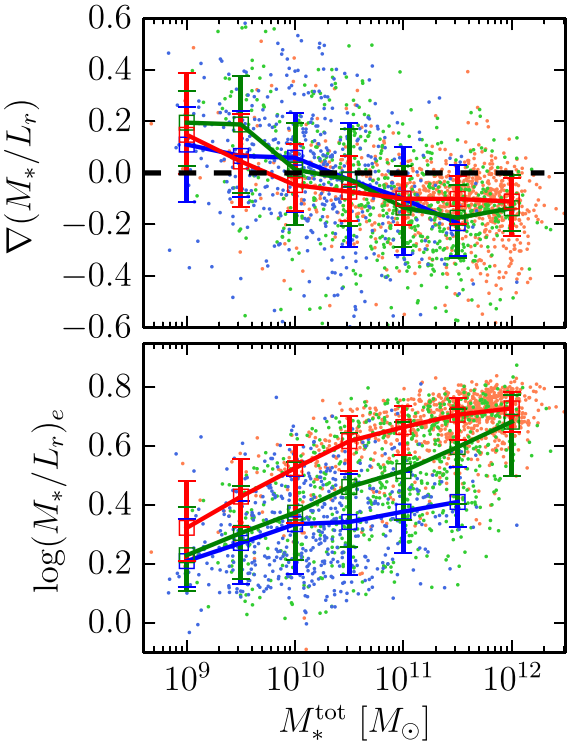

Figure 3. The logarithmic gradients of M_*/L_r (top panel) defined in equation (2) and the luminosity weighted mean values of M_*/L_r inside one effective radius, i.e. $\log(M_*/L_r)_e$ (bottom panel) as a function of galaxy stellar mass with different morphologies. The red, green, and blue points in each panel correspond to the ETGs, bulge+disc LTGs, and pure-disc LTGs, respectively. The median M_*/L_r gradients in a set of mass bins for the three types of galaxies are also shown by open boxes with errors labelled in the same colours as the data points. The error bars indicate the 16th and 84th percentiles for each mass bin. The width of each mass bin is 0.5 dex. Only those mass bins with at least three galaxies inside are plotted. The dashed line in the top panel shows $\nabla(M_*/L_r) = 0$, which helps present when the median gradient reverts from positive to negative.

et al. 2015; Yan et al. 2016), we cannot derive the whole 2D mass distribution by only using MaNGA data. As shown in the top panel, massive galaxies with total stellar mass larger than $10^{11}M_\odot$ have negative gradients with median values in the range $[-0.2, -0.15]$, which is consistent with results from Szomoru et al. (2013), Newman et al. (2015), Li et al. (2018), and Sonnenfeld et al. (2018). In particular, Li et al. (2018) used the same approach and MaNGA data but with a different galaxy sample, and our results are consistent with each other. The gradients become shallower with lower stellar mass for galaxies with $M_*^{\rm tot} \leq 10^{10}M_\odot$, and this trend is similar to that found in Tortora et al. (2011). For the $\nabla(M_*/L_r)$-mass correlations, all three types of galaxies show no significant difference. Whether pure-disc LTGs have a similar formation scenario as elliptical and bulge-dominated galaxies requires further exploration.

The difference between ETGs and bulge+disc LTGs is reflected by the luminosity-weighted mean M_*/L_r inside the galaxy half-light radius $\log(M_*/L_r)_e$ versus galaxy stellar mass plot shown in the bottom panel of Fig. 3. This correlation is similar to that of $\log(M_*/L_r)_e$ versus velocity dispersion as shown fig. 5 of Li et al. (2018). With increasing galaxy stellar mass or velocity dispersion, galaxies tend to have higher M_*/L_r, in which ETGs have the largest values, pure-disc LTGs have the smallest, while those of bulge+disc LTGs lie in between.

Fig. 4 presents another way of analysing the radial M_*/L_r profiles, by using the averaged radial M_*/L_r profiles for the three kinds of galaxies at different mass bins to study their evolution trends. With increasing stellar mass, the slopes of those radial profiles are positive for low mass bins and become negative for massive bins, presenting similar trends as shown in the top panel of Fig. 3. At the same time, the averaged M_*/L_r in each mass bin also increase with increasing galaxy mass, which is consistent with the bottom panel of Fig. 3.

To explore the evolution details of these galaxies, we first show $\nabla M_*/L_r$ as a function of age and metallicity gradients in both the luminosity- and mass-weighted cases in Fig. 5. Since the M_*/L of a spectrum is mainly determined by its stellar age, as a natural consequence, $\nabla M_*/L_r$ correlates tightest with the age gradient (panels a and c) rather than the metallicity gradient as shown in panels (b) and (d). The M_*/L_r gradients correlate with the mass-weighted stellar age gradients (panel c) more tightly than the luminosity-weighted ones (panel a). For all three kinds of galaxies, their $\nabla M_*/L_r$ increases with the stellar mass-weighted age gradient ∇t_M in a consistent way and the trends are close to the diagonal line (panel c). For the luminosity-weighted case (panel a), the $\nabla M_*/L_r$ versus the luminosity-weighted age gradient $\nabla(t_L)$ trends are largely biased away from the diagonal line, with pure-disc LTGs have the larger biases than ETGs and bulge+disc LTGs. This could be caused by stronger star formation happening in pure-disc LTGs than the other two kinds of galaxies.

At a certain stellar age, stellar spectra with larger metallicities also have higher M_*/L_r (e.g. fig. 2 of Ge et al. 2019). This also explains the positive correlation between $\nabla M_*/L_r$ and metallicity gradient ∇[M/H], which is clearly weaker than that between the $\nabla M_*/L_r$ and ∇t, as shown in panels (b) and (d) of Fig. 5. Compared to the monotonically increasing trend in the mass-weighted case shown in panel (d), the weakly increasing trend for $\nabla M_*/L_r$ as a function of $\nabla[\mathrm{M/H}]_L$ (panel b) becomes flat for bulge+disc LTGs and even inverts for pure-disc LTGs when $\nabla[\mathrm{M/H}]_L > 0$. Again, this might also be caused by different star formation strengths.

Since star formation can affect the $\nabla(M_*/L_r)$ estimates, Fig. 6 is plotted showing the variation in galaxy sSFR with $\nabla(M_*/L_r)$. Galaxies with $(\mathrm{sSFR})_e < 10^{-3}$ Gyr^{-1} (solid circles in the left-hand panel) can be classified by the origin of Hα emission lines, with ionization not only from SFR, but also hot low-mass evolved stars and weak active galactic nuclei (AGNs; e.g. Stasińska et al. 2008; Cid Fernandes et al. 2011). From the WHAN diagram of Cid Fernandes et al. (2011), passive galaxies and LINER dominate the weak emission line systems, which means that galaxies in the middle panel of Fig. 6 are dominated by these two kinds of objects. Hα emission lines ionized by hot low-mass evolved stars and weak AGNs would not support a strong correlation between sSFR and M_*/L_r gradients. These passive galaxies with weak SFR have little effect on the $\nabla M_*/L_r$ estimates. Hence we obtain a slope of zero (red line in the middle panel) of their correlations. For star-forming galaxies with $(\mathrm{sSFR})_e > 10^{-3}$ Gyr^{-1}, a clear anticorrelation between ∇sSFR and $\nabla M_*/L_r$ appears (blue line in the right-hand panel). By performing the linear correlation analysis with LTS_LINEFIT, we determine that this anticorrelation has a slope of -0.167 ± 0.009 with a scatter of 0.172 ± 0.005. The two kinds of correlation behaviours indicate that star formation in passive galaxies contributes little to the measurements of stellar ages and M_*/L_r. However, for star-forming galaxies, a higher sSFR can produce a younger luminosity-weighted age and hence smaller M_*/L_r. This means that for a galaxy with a positive sSFR gradient and $(\mathrm{sSFR})_e > 10^{-3}$ Gyr^{-1}, the galaxy

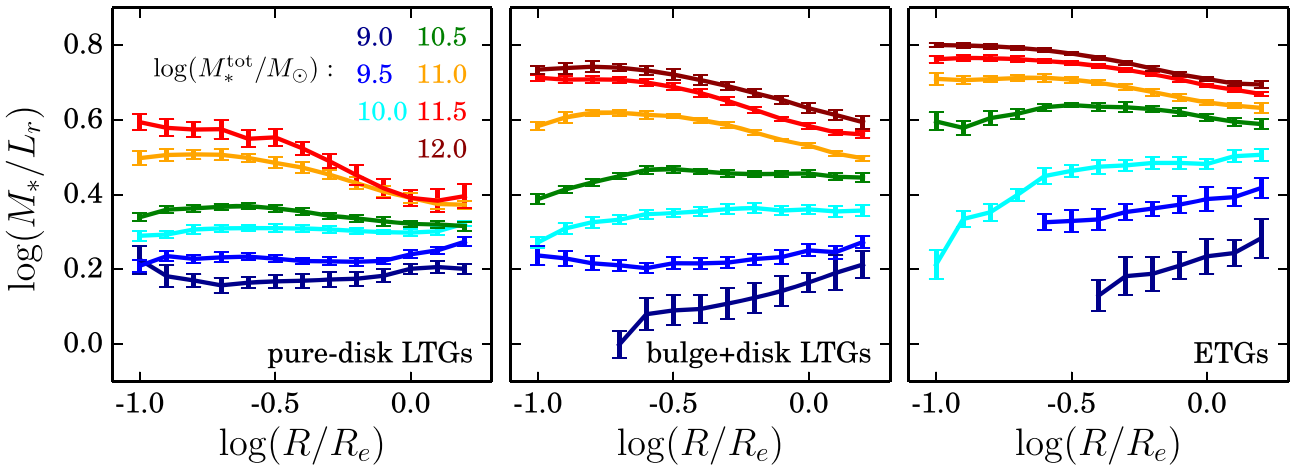

Figure 4. The averaged radial M_*/L_r profiles for different galaxy types and mass bins corresponding to Fig. 3. Panels from left to right show results for pure-disc LTGs, bulge+disc LTGs, and ETGs. Colours from dark blue to dark red represent the galaxy mass from $\log(M_*^{\rm tot}/M_\odot) = 9.0$ to 12.0, as labelled in the left-hand panel. By setting the galaxy radii ranging from 0.1 to 1.5 R_e evenly sampled logarithmically, with each radial bin having a width of 0.1 dex, we calculate the averaged $\log(M_*/L_r)$ and the corresponding uncertainty only if over 50 per cent of galaxies included in this bin have been spatially resolved. Considering that the typical seeing of MaNGA observations is 1.5 arcsec, the inner ∼3 data points are mostly affected by the seeing effect than those outside radial bins.

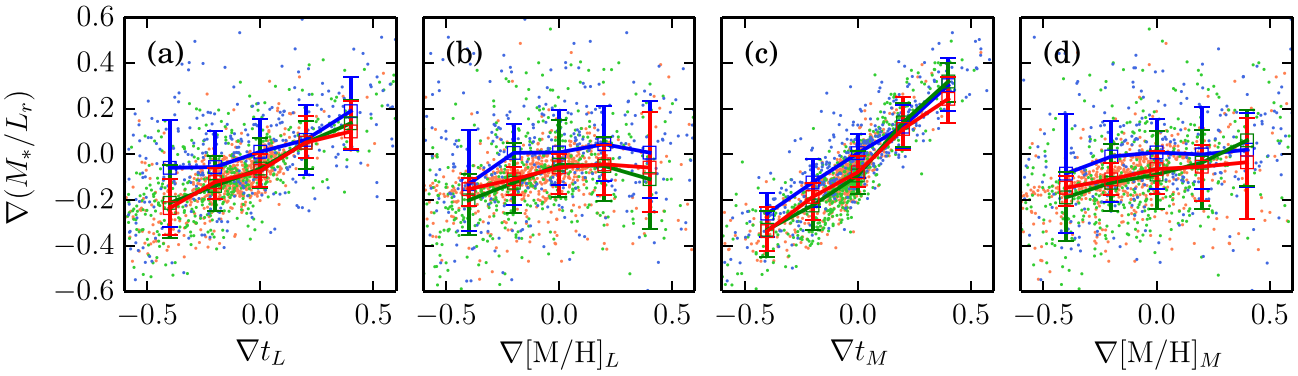

Figure 5. Correlations between M_*/L_r gradients and other stellar population parameters: gradients of luminosity-weighted stellar age (t_L, panel a), luminosity-weighted stellar metallicity ($[M/H]_L$, panel b), mass-weighted stellar age (t_M, panel c), and mass-weighted stellar metallicity ($[M/H]_M$, panel d). ETGs, LTGs with and without a central bulge are shown in red, green, and blue colours, respectively. The median values in each age or metallicity gradient bins are shown by open boxes and the associated error bars (16th and 84th percentiles) in the same colour correspondingly.

tends to have a more negative ∇t_L and $\nabla(M_*/L_r)$. Therefore, the anticorrelation shown in the right-hand panel of Fig. 6 explains why the $\nabla(M_*/L_r)$ as a function of ∇t_L presents different trends from that of ∇t_M as shown in panels (a) and (c) of Fig. 5, respectively.

According to the results shown in the bottom panel of Fig. 3, bulge+disc LTGs lie between the ETGs and pure-disc LTGs. In the middle and right-hand panels of Fig. 6, galaxies with different $\rm sSFR_e$ have their $\nabla(M_*/L_r)$ and ∇sSFR correlated in two ways. To understand further how ETGs and LTGs evolve with their mass, we explore the stellar population gradients in terms of their total stellar mass $M_*^{\rm tot}$.

As shown in Fig. 7, both the luminosity-weighted (∇t_L, panel a) and mass-weighted (∇t_M, panel c) age gradients show similar trends with increasing stellar mass as $\nabla(M_*/L_r)$ (top panel of Fig. 3), because of their positive correlations as presented in panels (a) and (c) of Fig. 5. The $\nabla[M/H]_L$ (panel b) and $\nabla[M/H]_M$ (panel d) show a systematic decreasing trend with increasing galaxy mass, although with a large scatter when taking the 16th and 84th percentiles as error bars. ETGs, with the largest $(M_*/L_r)_e$ (bottom panel of Fig. 3), tend to have lower sSFR than LTGs, and pure-disc LTGs have the largest sSFR in each mass bin, with bulge+disc LTGs lying in between (panel e). The median values of ∇E(B − V) (panel f) and ∇SFR (panel g) are consistent with each other and fluctuate around zero. The ∇SFR distributions have larger scatters than that of the E(B-V) gradients, especially for ETGs and bulge+disc LTGs. Even though we have improved the spectra S/N by spatially stacking spectra, this step mainly improves the robustness of E(B-V) estimates resulting from stellar population analysis. The Hα emission lines are still weak compared to the continua due to the lower SFR of ETGs and bulge-dominant LTGs, hence Hα-based ∇SFR values show larger scatter than that of ∇E(B − V). The age, metallicity, and M_*/L_r gradients have weakly decreasing trends with increasing galaxy mass. This can be explained by the correspondingly increased sSFR gradients as shown in panel (h).

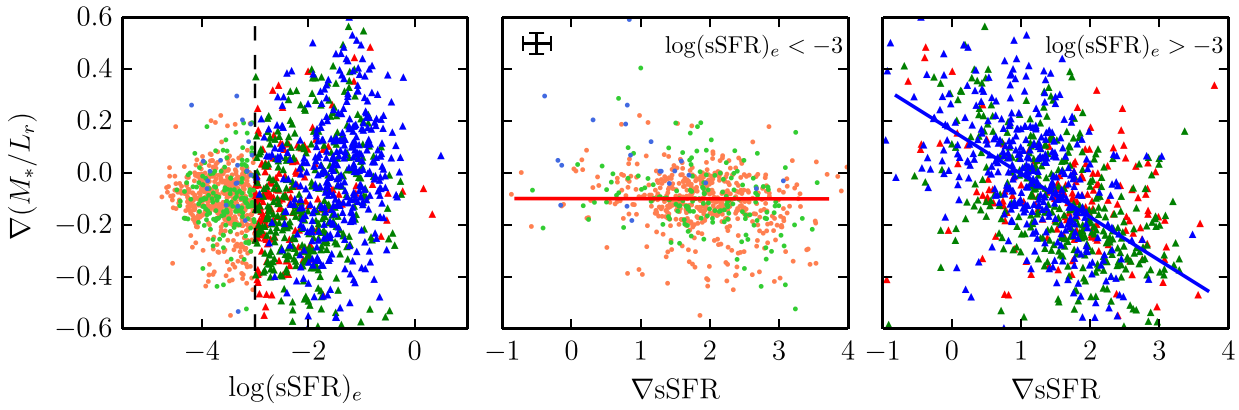

Figure 6. The M_*/L_r gradients as a function of sSFR inside a galaxy's half-light radius log (sSFR)$_e$ (left-hand panel) and ∇sSFR for log (sSFR)$_e$ < −3 (middle panel) and log (sSFR)$_e$ > −3 (right-hand panel) cases. The red, green, and blue points correspond to the ETGs, bulge+disc LTGs, and pure-disc LTGs, respectively. The vertical dashed line in the left-hand panel shows the criterion of log (sSFR)$_e$ = −3. Here we especially label those galaxies with log (sSFR)$_e$ > −3 by triangles in the corresponding darker colours. In the middle panel, galaxies with log (sSFR)$_e$ < −3 are plotted to present the $\nabla(M_*/L_r)$ as a function of ∇sSFR, and a linear fitting of these points are shown in red solid line with a slope of 0.0. The top-left horizontal and vertical error bars show the median errors of ∇sSFR and $\nabla(M_*/L_r)$ of the galaxy sample, respectively. The right-hand panel plots those galaxies with log (sSFR)$_e$ > −3, and has the linear fitting result overlapped as a blue solid line with a slope of −0.167 ± 0.009 and scatter of 0.172 ± 0.005 obtained from the LTS_LINEFIT correlation analysis.

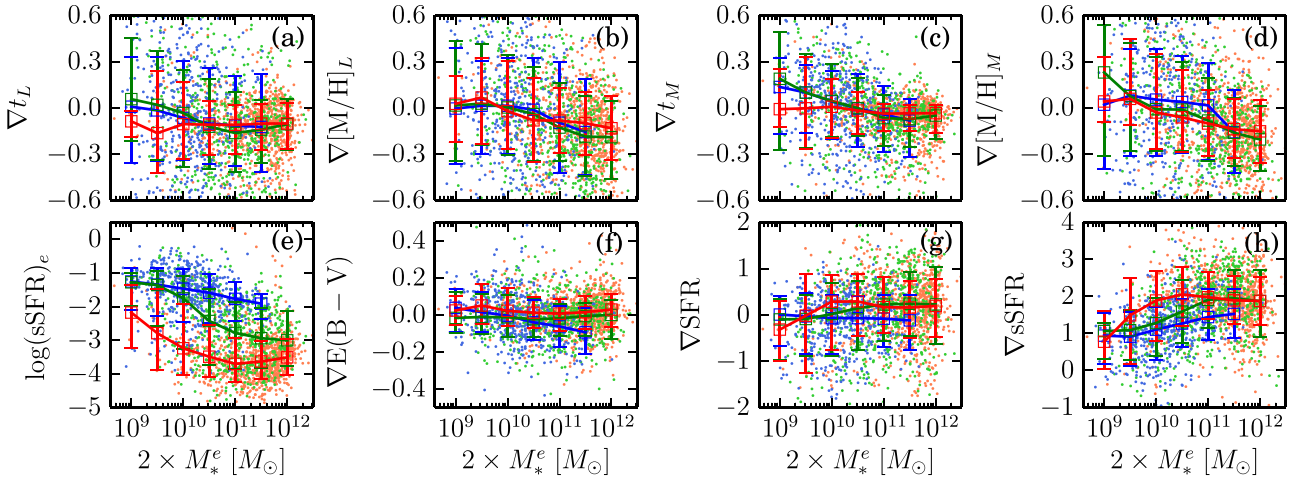

Figure 7. Galaxy properties as a function of stellar mass. Panels from (a) to (h) show ∇t_L, ∇[M/H]$_L$, ∇t_M, ∇[M/H]$_M$, log (sSFR)$_e$, ∇E(B-V), ∇SFR, and ∇sSFR in terms of the galaxy stellar mass $M_*^{\rm tot} = 2 \times M_*^e$. As shown in Fig. 3, the red, green, and blue points, and also the corresponding median value with error bars represented by 16th and 84th percentiles show the results of ETGs, LTGs with and without bulges, respectively.

3.2 M_*/L_r-colour relations

For galaxies in our sample, we take the M_*/L_r values for all the spatially rebinned spaxels, and use them to investigate potential relationships between M_*/L_r and colours. Here we take $g - r$, $r - i$, and $g - i$ colours from the SDSS *gri* bands for analyses. By applying the PPXF fitted E(B-V) dust extinction correction to the *gri* band luminosities, all three colours are dust extinction corrected.

Fig. 8 shows M_*/L_r as a function of SDSS $g - r$ (left-hand column), $r - i$ (middle column), and $g - i$ colours (right-hand column) under the assumption of a universal Salpeter IMF. The dashed line in each panel shows the linear fitting result of the M_*/L_r-colour correlation, with the detailed parameters listed in Table 1. In each panel, we can see a tight linear correlation (e.g. Bell & de Jong 2001) for ∼80 per cent of spaxels (surrounded by the first and second central contours). Other works (e.g. García-Benito et al. 2019), find a similar result. Compared to Bell & de Jong (2001), which studied the M_*/L-colour relations by assuming different galaxy evolution models, our results provide the statistical M_*/L-colour correlation coefficients of galaxies with real SFHs at redshift range $z \sim [0, 0.15]$ (Bundy et al. 2015). Spectra from IFS observations with the FoV covering $\geq 1.5R_e$ also contain more complex SFHs than single observed spectra only focusing on the central 3 arcsec diameter fibre (e.g. Bell et al. 2003). Therefore, the correlation coefficients of M_*/L_r versus $g - r$, $r - i$, and $g - i$ colour relations vary slightly but are roughly consistent with that of Bell et al. (2003).

M_*/L_r not only correlates well with galaxy colours, but also with luminosity-weighted stellar ages (t_L, see the top three panels of Fig. 8). However, for the mass-weighted stellar age (t_M) case (the middle row of Fig. 8), the correlation behaviours among them are different from that of the t_L case. Spaxels with similar t_M can have

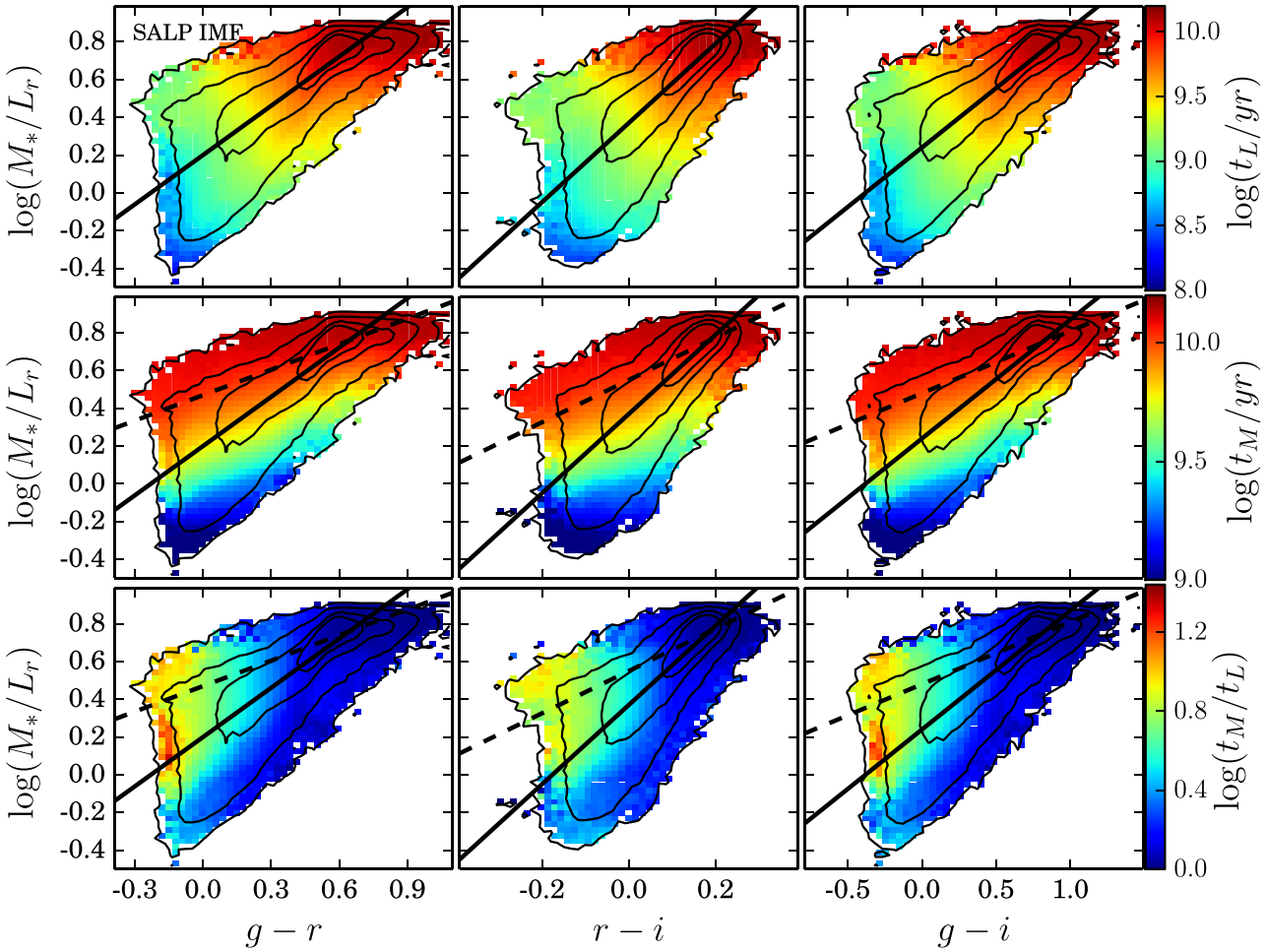

Figure 8. The M_*/L_r and colour relations after assuming a universal Salpeter IMF. Panels from left to right correspond to the correlations with SDSS $g-r$, $r-i$, and $g-i$ colours, with all the colours are dust extinction corrected based on the fitted E(B-V) in PPXF fitting. In each panel, the black contours show the density distribution of pixels with number density larger than 10, which means that all the pixels shown here have S/N>3 in the case of Poisson noise distribution. We fit the correlation by $\log(M_*/L_r) = a + b \times$ colour, and show the fitting result as the black solid lines. Those pixels with colours from blue to red represent the mean luminosity-weighted (top three panels) or mass-weighted (middle three panels) stellar ages from young to old. In the middle three panels, the black dashed lines show linear fitting results of those spectra with mass-weighted stellar age $t_M > 10$ Gyr. In the bottom three panels, we present the age difference between the mass- and luminosity-weighted stellar ages, i.e. $\Delta\log t = \log(t_M/t_L)$. Blue colours indicate SFHs dominated by a single burst while redder colours correspond to more complex SFHs with higher fraction of newly formed stars.

Table 1. The M_*/L_r as a function of colour at fixed Salpeter IMF assumption.

Colour	a	b	a_o	b_o
$g-r$	0.20	0.87	0.47	0.45
$r-i$	0.37	2.10	0.55	1.12
$g-i$	0.24	0.63	0.48	0.33

Note. For the fitting function of $\log(M_*/L_r) = a + b \times$ colour. The subscript o represents the fitting results of those spectra with older mass-weighted stellar ages ($t_M > 10$ Gyr).

different colours. This is due to the varied star formation histories that have occurred (e.g. Bell et al. 2003; Gallazzi & Bell 2009). As studied in Yesuf et al. (2014) and Pawlik et al. (2018), post-starburst galaxies can be divided into several types based on the fraction and appearance time of starbursts in the star formation history (SFH). In the bottom row of Fig. 8, we plot the age difference of each spectrum $\Delta\log t = \log(t_M/t_L)$ as an indicator for reflecting the contribution of newly formed stars to the whole SFH. For example, post-starburst galaxies with their recent star bursts happening in the last 1 Gyr can change the galaxy colours from red to blue, but the t_M can still be ∼10 Gyr, and is largely biased from an exponential SFH. In the bottom panels of Fig. 8, those pixels in red show galaxies with SFHs having the strongest recent starbursts. Spaxels with similar SFHs as post-starburst galaxies can lie on the top-left of the density distribution in each panel, i.e. spaxels with a little bit smaller M_*/L_r, $t_M \sim 10$ Gyr, and blue colours, as shown in the middle row of Fig. 8. However, their age differences are larger than those with the same M_*/L_r with redder galaxy colours, or the same galaxy colours with lower M_*/L_r.

Those spaxels with large age difference are not insignificant for the current sample. Fig. 9 shows the $\Delta\log t$ distribution for all rebinned spectra of our galaxy sample, in which ∼16 per cent of the total spaxels have $\Delta\log t > 0.5$ dex, and ∼5 per cent of them have $\Delta\log t > 1.0$ dex, which means that their newly formed stars

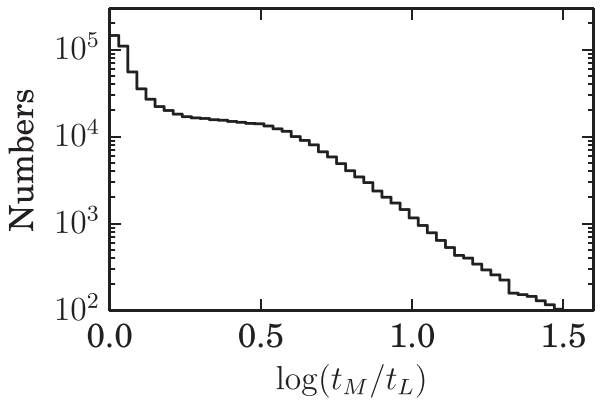

Figure 9. Number distribution of $\Delta\log t = \log(t_M/t_L)$ for 690,944 spectra from the Voronoi 2D binning of 2051 galaxies, in which 111 613 spectra (∼16 per cent) have $\Delta\log t > 0.5$, and 6777 spectra (∼1 per cent) have $\Delta\log t > 1.0$.

can have a significant effect on changing of spectral shape and galaxy colours.

The correlation coefficients of those spaxels with stellar age older than 10 Gyr are also listed in Table 1, and are systematically flattened compared to all spaxels. A similar result is found by Gallazzi & Bell (2009) (see their fig. 11), which has less complex SFHs assumed than the observed MaNGA data. Our results actually complement the missing top-left part in their fig. 11 that has blue colours but old populations with high M_*/L_r.

With the statistical analyses on the effect of complex SFHs to the M_*/L_r-galaxy colour relations, the correlation slopes obtained by different works are mainly determined by their galaxy types. For local galaxies, the slopes obtained in different works are no flatter than the b_o listed in Table 1, but the detailed values could vary due to the different selection criteria of their galaxy samples, which indicates that varied SFH distributions are covered in the M_*/L-colour relations (e.g. Bell & de Jong 2001; Bell et al. 2003; Gallazzi & Bell 2009; García-Benito et al. 2019).

4 DISCUSSION

4.1 Comparison with previous works

Tortora et al. (2011) performed SED fitting of SDSS *ugriz* bands for 50 000 galaxies and found that galaxies of different types show different behaviours for their M_*/L gradients as a function of stellar mass. For LTGs, gradients steepen negatively with increasing mass, while for ETGs, gradients first decrease with increasing mass up to $\sim 10^{10.3} M_\odot$, and then increase with increasing mass. The advantage of using photometric data with stellar population analysis is that galaxy images can be obtained with much less observation time and higher S/N and larger FoV than that for IFU observations. However, the fitted results are contaminated by both emission line (e.g. Hα) contributions to different bands (especially for LTGs), and lack of absorption lines, which introduces large uncertainties caused by the degeneracy between age, metallicity, and dust extinction.

Compared to the results obtained from SED fittings (Tortora et al. 2011), MaNGA data provide us with spectral resolution ($R \sim 2000$; Smee et al. 2013) high enough to resolve absorption lines and with wide enough spectral wavelength coverage (3600–10 500 Å; Bundy et al. 2015) to perform reliable stellar population analyses, if we choose a suitable spectral fitting code and SSP library. For the PPXF code used in this work, the dust extinction uncertainty is less than 0.01 mag for galaxy spectra with age $t > 0.1$ Gyr, as shown in fig. 4 of Ge et al. (2018). This indicates that the degeneracy between stellar age and dust extinction in the SED fitting process cannot contaminate our analyses of MaNGA data if the assumed dust reddening curve is precise enough. However, many efforts focusing on the dust reddening curve show that the dust-star geometry is complex and that star-forming regions even require a two-component dust model for explanation (e.g. Charlot & Fall 2000; Wilkinson et al. 2015, 2017; Li et al. 2020, 2021).

The sample size of Tortora et al. (2011) is, however, larger than the number of galaxies selected in our work, and their galaxies are fainter than ours. The photometrically selected galaxy sample can have galaxy stellar masses ranging from $10^{7.7} M_\odot$ to the most massive galaxies (see their fig. 3 for details) in the SDSS photometric survey. The current MaNGA survey has smaller mass coverage (see Fig. 3) than in the Tortora sample.

4.2 Previous usage of M/L gradients in dynamical models

In external galaxy dynamical modelling, e.g. Jeans equations modelling (Cappellari 2008), orbit based modelling (Schwarzschild 1979), or particle-based modelling (Syer & Tremaine 1996) in the past it was common to adopt mass-follow-light models assuming a constant M_*/L (e.g. van der Marel 1991; Cappellari et al. 2006; Long & Mao 2012). It was motivated by simplicity and by the fact that the dynamical models were targeting central parts of early-type galaxies, where population gradients are modest.

Some papers assessed the influence of M_*/L gradients on masses of supermassive black holes (e.g. Cappellari et al. 2002; McConnell et al. 2013; Thater et al. 2017, 2019). They found that ignoring M_*/L variations in mass-follow-light models can lead to biases in the black hole masses.

However, one fact that is not always appreciated is that the stellar surface brightness (as opposed to the stellar mass density) remains the best approximation for the stellar-tracer population, even when M_*/L gradients are present. It implies that one can still correctly model the galaxies' total density, without distinguishing what fraction is due to the stellar mass and which one is due to the dark matter. In this case, one treats the stars only as a tracer population orbiting in the total gravitational potential and recovers reliable total densities without the need to know the M_*/L gradients (e.g. Cappellari et al. 2015; Mitzkus, Cappellari & Walcher 2017; Poci, Cappellari & McDermid 2017).

On the other hand, focusing on the total density alone, in the presence of significant M_*/L gradients, prevents one from measuring unbiased dark matter profiles or estimating the stellar M_*/L (and IMF). For this, one has to explicitly include the M_*/L gradients in the mass models as done in more recent studies based on IFS data (Li et al. 2017; Mitzkus et al. 2017; Poci et al. 2017). In this situation, our assessment of systematic trends of M_*/L gradients in galaxies becomes relevant.

4.3 Effect of radial IMF variations to $\nabla M_*/L$ measurements

Once a galaxy has radially varying IMFs (see a review by Smith 2020), then the M_*/L gradients will become more negative than the constant IMF case as assumed in this work. Fig. 10 shows the M_*/L_r difference between the Salpeter and Chabrier (or Kroupa) IMFs in the left-hand (or right-hand) panel, which means that, if we assume a galaxy has a Salpeter IMF at $0.1R_e$ and a Chabrier (or Kroupa) IMF at $1R_e$, the corresponding M_*/L_r difference shown in the left-hand

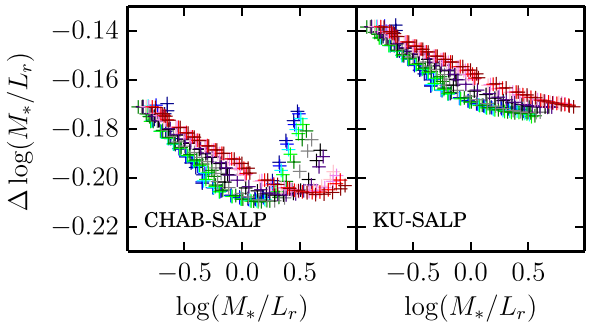

Figure 10. The M_*/L_r differences ($\Delta(M_*/L_r)$) as a function of M_*/L_r in the Salpeter IMF for the Vazdekis/MILES model based SSP libraries. The left-hand panel shows the $\Delta(M_*/L_r)$ between the Chabrier and Salpeter IMFs (i.e. CHAB−SALP), while the right-hand panel presents that between Kroupa Universal and Salpeter IMFs (i.e. KU−SALP). In each panel, the 12 kinds of stellar metallicities from poor ([M/H] = −2.27) to rich (0.4) are labelled with colours from blue to red, respectively.

(or right-hand) panel is exactly the M_*/L_r gradient that is further steepened (see detailed discussion in García-Benito et al. 2019).

If M_*/L-colour relations are applied to convert the galaxy colours to M_*/L, the correlation slopes are also steepened by potential radial IMF variations, leading to another difference with a constant M_*/L approach. For example, Li et al. (2020) in modelling M87 utilized a M_*/L profile produced by Sarzi et al. (2018), which revealed a strong negative IMF gradient by taking the IMF-sensitive absorption line features for stellar population analyses, and caused over a factor 2 increase in M_*/L compared to the case of a Milky Way IMF.

5 CONCLUSIONS

Using a sample of 2051 face-on galaxies selected from the MaNGA sample released in SDSS DR15, we have investigated how galaxy M_*/L_r gradients depend on morphology under the assumption of a universal Salpeter IMF. We exclude galaxies that are merging, barred, highly inclined ($i > 45°$), or have insufficient S/N to ensure robust stellar population analyses for calculations of stellar population gradients. We classify our galaxies into three groups: (1) ETGs, (2) LTGs with both bulge and disc components (bulge+disc LTGs), and (3) LTGs only having one disc component (pure-disc LTGs).

The M_*/L_r gradients for all the three types of galaxies have similar trends as a function of galaxy stellar mass, i.e. $\nabla(M_*/L_r)$ reverts from positive (∼0.1) to negative (∼−0.1) when galaxy masses increasing from the lowest ($\sim 10^9 M_\odot$) to the highest ones ($\sim 10^{12} M_\odot$). With increasing galaxy stellar mass, the luminosity weighted M_*/L_r inside a half-light radius $\log(M_*/L_r)_e$ also increases, with the trends similar to that found in the velocity dispersion σ_e versus $\log(M_*/L_r)_e$ correlations (e.g. Li et al. 2018). The age gradients as a function of $M_*^{\rm tot}$ show similar trend as $\nabla M_*/L_r$, while the metallicity gradients systematically decrease with increasing $M_*^{\rm tot}$. For $\log(M_*/L_r)_e$ in different mass bin, ETGs have the largest values, and pure-disc LTGs have the smallest, while bulge+disc LTGs lie in between. Correspondingly, the sSFR inside $1R_e$ ($\rm sSFR_e$) is the lowest for ETGs, and the highest for pure-disc LTGs.

$\nabla(M_*/L_r)$ correlates with mass-weighted stellar age gradients (∇t_M) more so than other parameters. Its correlation with luminosity-weighted age gradients (∇t_L) is significantly affected by the star formation when $\rm sSFR_e$ is greater than $10^{-3}\,\rm Gyr^{-1}$, where these galaxies have their $\nabla(M_*/L_r)$ decreasing with increasing ∇sSFR. This indicates that a stronger sSFR in the outer radii leads to smaller t_L and M_*/L_r, and hence more negative ∇t_L and $\nabla(M_*/L_r)$. The weak positive correlations between $\nabla(M_*/L_r)$ and metallicity gradients are also affected by the galaxy star formation rate.

For the M_*/L_r-colour relations, old populations with stellar age older than 10 Gyr tend to have shallower correlation slopes than the global ones. In particular, the conversion of M_*/L from galaxy colours for post-starburst galaxies should be very carefully calculated when their SFHs include old populations dominating the stellar mass but newly formed stars dominating the luminosity.

ACKNOWLEDGEMENTS

We would like to thank the anonymous referee for the suggestions that helped us to improve this paper. We thank Cheng Li for helpful discussions. This work is supported by the Beijing Municipal Natural Science Foundation (No. 1204038 to JG), by the National Key Research and Development Program of China (No. 2018YFA0404501 to SM), by the National Natural Science Foundation of China (NSFC) under grant numbers 11903046 and U1931110 (JG), 11333003 and 11761131004 (SM), and 11390372 (SM, YL), and by the National Key Program for Science and Technology Research and Development (Grant No. 2016YFA0400704 to YL). RY acknowledges support by National Science Foundation grant AST-1715898.

Funding for the Sloan Digital Sky Survey IV has been provided by the Alfred P. Sloan Foundation, the U.S. Department of Energy Office of Science, and the Participating Institutions.

SDSS-IV acknowledges support and resources from the Center for High Performance Computing at the University of Utah. The SDSS website is www.sdss.org.

SDSS-IV is managed by the Astrophysical Research Consortium for the Participating Institutions of the SDSS Collaboration including the Brazilian Participation Group, the Carnegie Institution for Science, Carnegie Mellon University, Center for Astrophysics | Harvard & Smithsonian, the Chilean Participation Group, the French Participation Group, Instituto de Astrofísica de Canarias, The Johns Hopkins University, Kavli Institute for the Physics and Mathematics of the Universe (IPMU) / University of Tokyo, the Korean Participation Group, Lawrence Berkeley National Laboratory, Leibniz Institut für Astrophysik Potsdam (AIP), Max-Planck-Institut für Astronomie (MPIA Heidelberg), Max-Planck-Institut für Astrophysik (MPA Garching), Max-Planck-Institut für Extraterrestrische Physik (MPE), National Astronomical Observatories of China, New Mexico State University, New York University, University of Notre Dame, Observatário Nacional / MCTI, The Ohio State University, Pennsylvania State University, Shanghai Astronomical Observatory, United Kingdom Participation Group, Universidad Nacional Autónoma de México, University of Arizona, University of Colorado Boulder, University of Oxford, University of Portsmouth, University of Utah, University of Virginia, University of Washington, University of Wisconsin, Vanderbilt University, and Yale University.

DATA AVAILABILITY

The data underlying this article will be shared on reasonable request to the corresponding author.

REFERENCES

Aguado D. S., Ahumada R., Almeida A. et al., 2019, ApJS, 240, 23
Alton P. D., Smith R. J., Lucey J. R., 2018, MNRAS, 478, 4464
Auger M. W. et al., 2010, ApJ, 721, L163
Bacon R. et al., 2014, Messenger, 157, 13

Bell E. F. et al., 2003, ApJS, 149, 289
Bell E. F., de Jong R. S., 2001, ApJ, 550, 212
Bezanson R. et al., 2009, ApJ, 697, 1290
Bundy K. et al., 2015, ApJ, 798, 7
Calzetti D. et al., 2000, ApJ, 533, 682
Cappellari M., 2002, MNRAS, 333, 400
Cappellari M., 2008, MNRAS, 390, 71
Cappellari M., 2016, ARA&A, 54, 597
Cappellari M., 2017, MNRAS, 466, 798
Cappellari M., Copin Y., 2003, MNRAS, 342, 345
Cappellari M., Emsellem E., 2004, PASP, 116, 138
Cappellari M. et al., 2002, ApJ, 578, 787
Cappellari M. et al., 2006, MNRAS, 366, 1126
Cappellari M. et al., 2012, Nature, 484, 485
Cappellari M. et al., 2013, MNRAS, 432, 1709
Cappellari M. et al., 2015, ApJ, 804, L21
Chabrier G., 2003, PASP, 115, 763
Charlot S., Fall S. M., 2000, ApJ, 539, 718
Cid Fernandes R. et al., 2011, MNRAS, 413, 1687
Ciotti L., Lanzoni B., Volonteri M., 2007, ApJ, 658, 65
Conroy C., 2013, ARA&A, 51, 393
Conroy C., van Dokkum P. G., Villaume A., 2017, ApJ, 837, 166
Cordier D., Pietrinferni A., Cassisi S., Salaris M., 2007, AJ, 133, 468
Domínguez Sánchez H., Huertas-Company M., Bernardi M., Tuccillo D., Fischer J. L., 2018, MNRAS, 476, 3661
Domínguez Sánchez H. et al., 2019, MNRAS, 489, 5612
Du C., Li N., Li C., 2019, Res. Astron. Astrophys., 12, 171
Eggen O. J., Lynden-Bell D., Sandage A. R., 1962, ApJ, 136, 748
Ferreras I. et al., 2013, MNRAS, 429, L15
Fischer J.-L., Domínguez Sánchez H., Bernardi M., 2019, MNRAS, 483, 2057
Gallazzi A., Bell E. F., 2009, ApJS, 185, 253
García-Benito R. et al., 2019, A&A, 621, A120
Ge J. et al., 2018, MNRAS, 478, 2633
Ge J., Mao S., Lu Y. et al., 2019, MNRAS, 485, 1675
Goddard D. et al., 2017, MNRAS, 466, 4731
Gonzalez Delgado R. M. et al., 2015, A&A, 581, A103
Harris C. R. et al., 2020, Nature, 585, 357
Hopkins P. F. et al., 2009, MNRAS, 398, 898
Hopkins P. F. et al., 2010, MNRAS, 401, 1099
Kennicutt R. C., 1998, ARA&A, 36, 189
Koleva M. et al., 2011, MNRAS, 417, 1643
Kroupa P., 2001, MNRAS, 322, 231
Kuntschner H. et al., 2010, MNRAS, 408, 97
Larson R. B., 1974, MNRAS, 166, 585
Li H. et al., 2017, ApJ, 838, 77
Li H. et al., 2018, MNRAS, 476, 1765
Li N. et al., 2020, ApJ, 896, 38
Li C. et al., 2020, MNRAS, 492, 2775
Li N., Li C., Mo H. et al., 2021, ApJ, 917, 72
Long R. J., Mao S., 2012, MNRAS, 421, 2580
Lu S. et al., 2020, MNRAS, 495, 4820
Martin-Navarro I. et al., 2018, MNRAS, 475, 3700
McConnell N. J. et al., 2013, ApJ, 768, L21
Mehlert D. et al., 2003, A&A, 407, 423
Mitzkus M., Cappellari M., Walcher C. J., 2017, MNRAS, 464, 4789
Naab T., 2013, in Thomas D., Pasquali A., Ferreras I., eds, Proc. IAU Symp. 295, The Intriguing Life of Massive galaxies. Cambridge University Press, Cambridge, p. 340
Newman A. B., Ellis R. S., Treu T., 2015, ApJ, 814, 26
Oliphant T. E., 2007, Comput. Sci. Eng., 9, 10
Oser L. et al., 2010, ApJ, 725, 2312
Oser L. et al., 2012, ApJ, 744, 63
Parikh T. et al., 2018, MNRAS, 477, 3954
Pawlik M. M. et al., 2018, MNRAS, 477, 1708
Pérez E. et al., 2013, ApJ, 764, L1
Pietrinferni A., Cassisi S., Salaris M., Castelli F., 2004, ApJ, 612, 168
Poci A., Cappellari M., McDermid R. M., 2017, MNRAS, 467, 1397
Rodriguez-Gomez V. et al., 2016, MNRAS, 458, 2371
Salpeter E. E., 1955, ApJ, 121, 161
Sanchez S. F. et al., 2012, A&A, 538, A8
Sarzi M., Spiniello C., La Barbera F., Krajnović D., van den Bosch R., 2018, MNRAS, 478, 4084
Schwarzschild M., 1979, ApJ, 232, 236
Smee S. A. et al., 2013, AJ, 146, 32
Smith R. J., 2020, ARA&A, 58, 577
Sonnenfeld A. et al., 2018, MNRAS, 481, 164
Spiniello C., Trager S., Koopmans L. V. E., Conroy C., 2014, MNRAS, 438, 1483
Spolaor M. et al., 2009, ApJ, 691, L138
Stasińska G. et al., 2008, MNRAS, 391, L29
Syer D., Tremaine S., 1996, MNRAS, 282, 223
Szomoru D. et al., 2013, ApJ, 763, 73
Thater S. et al., 2017, A&A, 597, A18
Thater S. et al., 2019, A&A, 625, A62
Thomas J. et al., 2011, MNRAS, 415, 545
Tortora C. et al., 2011, MNRAS, 418, 1557
van der Marel R. P., 1991, MNRAS, 253, 710
van Dokkum P. G., Conroy C., 2010, Nature, 468, 940
Vaughan S. P. et al., 2018, MNRAS, 479, 2443
Vaughan S. P., Houghton R. C. W., Davies R. L, Zieleniewski S., 2018a, MNRAS, 475, 1073
Vazdekis A. et al., 2010, MNRAS, 404, 1639
White S., Rees M., 1978, MNRAS, 183, 341
Wilkinson D. M. et al., 2015, MNRAS, 449, 328
Wilkinson D. M. et al., 2017, MNRAS, 472, 4297
Yan R. et al., 2016, AJ, 152, 197
Yesuf H. M. et al., 2014, ApJ, 792, 84
Zheng Z. et al., 2017, MNRAS, 465, 4572
Zhou S. et al., 2019, MNRAS, 485, 5256
Zibetti S. et al., 2020, MNRAS, 491, 3562
Zieleniewski S. et al., 2017, MNRAS, 465, 192

This paper has been typeset from a TEX/LATEX file prepared by the author.